The case for a high-redshift origin of GRB 100205A

A. A. Chrimes [1]★ A. J. Levan,[1,2] E. R. Stanway [1] E. Berger,[3] J. S. Bloom,[4]
S. B. Cenko,[5,6] B. E. Cobb,[7] A. Cucchiara,[8] A. S. Fruchter,[9] B. P. Gompertz,[1]
J. Hjorth,[10] P. Jakobsson,[11] J. D. Lyman,[1] P. O'Brien,[12] D. A. Perley [13]
N. R. Tanvir,[12] P. J. Wheatley [1] and K. Wiersema[1]

[1] *Department of Physics, University of Warwick, Gibbet Hill Road, Coventry CV4 7AL, UK*
[2] *Department of Astrophysics/IMAPP, Radboud University, Nijmegen, The Netherlands*
[3] *Harvard-Smithsonian Center for Astrophysics, 60 Garden Street, Cambridge, MA 02138, USA*
[4] *Department of Astronomy, University of California, Berkeley, CA 94720, USA*
[5] *NASA Goddard Space Flight Center, 8800 Greenbelt Road, Greenbelt, DMD 20771, USA*
[6] *Joint Space-Science Institute, University of Maryland, College Park, MD 20742, USA*
[7] *Department of Physics, The George Washington University, Washington, DC 20052, USA*
[8] *College of Science and Mathematics, University of the Virgin Islands, #2 Brewers Bay Road, Charlotte Amalie, USVI 00802*
[9] *Space Telescope Science Institute, 3700 San Martin Drive, Baltimore, MD 21218, USA*
[10] *Dark Cosmology Centre, Niels Bohr Institute, University of Copenhagen, Juliane Maries Vej 30, DK-2100 Copenhagen ø, Denmark*
[11] *Centre for Astrophysics and Cosmology, Science Institute, University of Iceland, Dunhagi 5, 107 Reykjavik, Iceland*
[12] *Department of Physics and Astronomy, University of Leicester, University Road, Leicester LE1 7RH, UK*
[13] *Astrophysics Research Institute, Liverpool John Moores University, 146 Brownlow Hill, Liverpool L3 5RF, UK*

ABSTRACT

The number of long gamma-ray bursts (GRBs) known to have occurred in the distant Universe ($z > 5$) is small ($\sim$15); however, these events provide a powerful way of probing star formation at the onset of galaxy evolution. In this paper, we present the case for GRB 100205A being a largely overlooked high-redshift event. While initially noted as a high-z candidate, this event and its host galaxy have not been explored in detail. By combining optical and near-infrared Gemini afterglow imaging (at $t < 1.3$ d since burst) with deep late-time limits on host emission from the *Hubble Space Telescope*, we show that the most likely scenario is that GRB 100205A arose in the range $4 < z < 8$. GRB 100205A is an example of a burst whose afterglow, even at $\sim$1 h post burst, could only be identified by 8-m class IR observations, and suggests that such observations of all optically dark bursts may be necessary to significantly enhance the number of high-redshift GRBs known.

Key words: gamma-ray burst: individual: 100205A – galaxies: high redshift.

1 INTRODUCTION

Long-duration gamma-ray bursts (GRBs) give rise to a synchrotron afterglow, detectable at optical wavelengths if sufficiently rapid and deep follow-up observations are made. A substantial fraction, however, lack such emission even when it would be expected from extrapolation of the X-ray spectral slope (Groot et al. 1998; Fynbo et al. 2001). When the X-ray to optical spectral slope, β_{OX}, is below the recognized threshold of 0.5, the event is classified as 'dark' (Jakobsson et al. 2004). This is typically evaluated at 11 h post-burst to avoid contamination from early-time effects including X-ray flares and plateaus. An alternative method uses $\beta_{OX} < \beta_X - 0.5$ to define darkness (van der Horst et al. 2009). There are

two primary causes for darkness in GRBs: attenuation by dust, or rest frame ultraviolet HI absorption at high redshift (e.g. Fruchter 1999; Levan et al. 2006; Perley et al. 2009, 2013; Greiner et al. 2011; Svensson et al. 2012; Zauderer et al. 2013; Chrimes et al. 2019; Higgins et al. 2019). The number of GRBs known at high-redshift ($z > 5$, in the epoch of reionization) is small ($\sim$15, from around 500 GRBs with a known or estimated redshift, Cenko et al. 2006; Grazian et al. 2006; Jakobsson et al. 2006; Kawai et al. 2006; Ruiz-Velasco et al. 2007; Salvaterra et al. 2009; Greiner et al. 2009; Tanvir et al. 2009; Cucchiara et al. 2011; Afonso et al. 2011; Castro-Tirado et al. 2013; Laskar et al. 2014; Jeong et al. 2014b; Chornock, Fox & Berger 2014b; Tanvir et al. 2018), and each one is valuable, as they provide insight into star formation in the low mass, low luminosity galaxies which power the epoch of reionization. Because they have small projected offsets from their hosts, high-redshift GRBs with a detected afterglow uniquely

★ E-mail: A.Chrimes@warwick.ac.uk

Table 1. Gemini/GMOS-S (*r*-band) and Gemini/NIRI afterglow observations. Afterglow magnitudes (or 3σ limits), corrected for Galactic extinction, and detection significance are listed in the final two columns. T_{obs} is the average time since burst trigger for the input exposures.

Filter	λ_{eff} (μm)	T_{obs} (h)	N_{exp}	Tot. Int. (s)	FWHM (arcsec)	Mag	σ
r	0.62	0.68	5	602.5	1.44	>25.2	–
Y	1.02	3.22	10	600	1.15	>23.5	–
K_{E1}	2.20	3.88	30	1800	0.58	23.45 ± 0.09	13.2
H	1.63	4.73	24	720	0.65	23.63 ± 0.26	3.69
J	1.25	5.48	17	510	0.63	24.29 ± 0.29	3.35
K_{E2}	2.20	30.32	28	1620	0.45	24.42 ± 0.16	6.40

allow us to place accurate, deep upper limits on the luminosities of the faintest, undetected galaxies, probing fainter galaxies than deep field studies (Berger et al. 2007; Tanvir et al. 2012; Trenti et al. 2012; McGuire et al. 2016). For those with the brightest afterglows, insight into the burst environment can be gained from absorption lines in their spectra (e.g. Kawai et al. 2006; Chornock et al. 2014a; Sparre et al. 2014; Hartoog et al. 2015).

In this paper, we present the case for dark GRB 100205A being a high-redshift event, undetected in the *r*-band, but faintly visible in the infrared, suggestive of the presence of the Lyman α break between the *r* and *J* bands at a redshift $z > 5$.

2 OBSERVATIONS, DATA REDUCTION, AND RESULTS

GRB 100205A ($T_{90} = 26$ s) was detected by the *Neil Gehrels Swift Observatory* (Gehrels et al. 2004) on 2010 February 5 (Racusin et al. 2010). The Burst Alert Telescope (BAT; Barthelmy et al. 2005) measured a fluence of $(4.0 \pm 0.7 \times 10^{-7})$ erg cm^{-2}, with a peak photon flux of (0.4 ± 0.1) cm^{-2} s^{-1} (15–150 keV, 90 per cent confidence errors). The enhanced X-Ray Telescope (XRT; Burrows et al. 2004) position was ra. 09h 25m 33.08s, dec. 31° 44′ 24.3″, with a 90 per cent error radius of 1.7 arcsec (Evans et al. 2009).[1]

The X-ray afterglow was rapidly identified, and ground-based observations were taken in the first hour after the burst. However, none of these early optical observations revealed a candidate optical afterglow (see Cobb, Cenko & Bloom 2010; Cucchiara et al. 2010; Malesani et al. 2010; Nicuesa et al. 2010; Perley et al. 2010; Tanvir et al. 2010; Urata, Huang & Im 2010), marking GRB 100205A as a dark burst (Malesani et al. 2010), and motivating further follow-up.

2.1 Gemini

Gemini/GMOS-S (Hook et al. 2004) observations in the *r*-band were obtained 40 min post trigger. These observations were reduced in the standard fashion within the Gemini IRAF environment, and did not yield an optical afterglow to a 3 σ limit of $R > 25.2$, the deepest upper limit on the optical light available.

Given this non-detection the burst location was subsequently imaged in the infrared by Gemini-N/NIRI (Hodapp et al. 2003) in the *Y*, *J*, *H*, and *K* bands starting at ∼2.4 h post burst, as shown in Table 1.

The data were reduced using standard procedures with the Gemini IRAF package, and care was taken to optimize bad pixel rejection. Cutouts of the reduced images around the GRB afterglow location are shown in Fig. 1. Also shown is a wider-field view, which includes
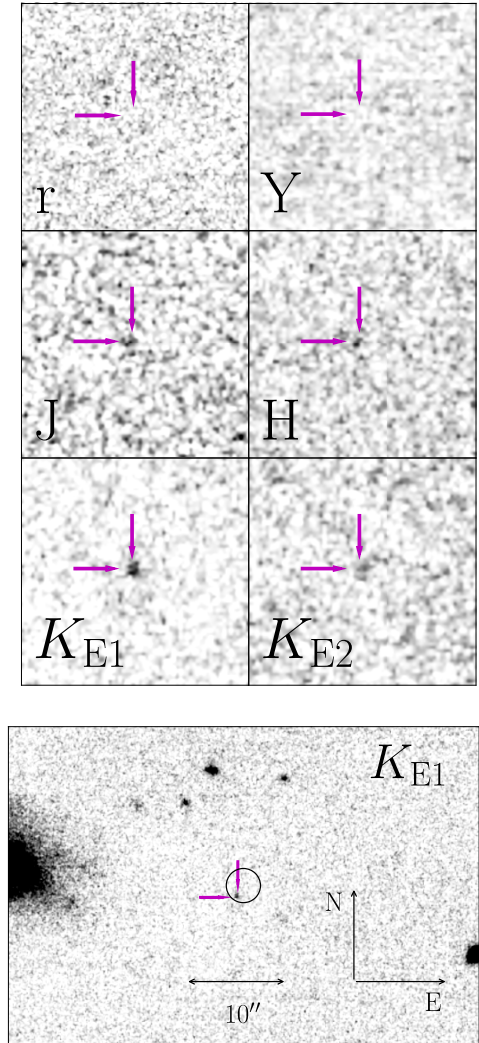
Figure 1. Image cutouts (4 arcsec × 4 arcsec) around the afterglow position for each set of Gemini observations. Numbering indicates whether data is from the first or second observation with that filter. Below these is wider area cutout to demonstrate the location of the burst with respect to a nearby large galaxy. Included here is the *Swift* enhanced XRT position, indicated by a black circle (with a 90 per cent error radius of 1.7 arcsec). All images have been smoothed with a 3 × 3 pixel Gaussian filter.

the *Swift* enhanced XRT position. The *K*-band numbering (K_{E1}, K_{E2}) refers to the first and second epochs of observation, which were approximately 1 d apart. The two epochs in *H* and *J* are sufficiently close in time that we have combined the data from these, where
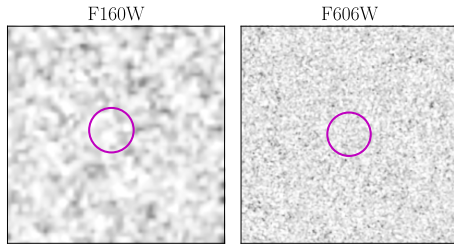
Figure 2. *HST* image stamps at the location of GRB 100205A, the images are smoothed with a 3×3 pixel Gaussian filter. The burst location is indicated in each image by a 0.4 arcsec radius circle. No host is detected down to 3σ magnitude limits of 26.7 and 27.1 for F160W and F606W, respectively.

that led to an improvement in signal-to-noise. Afterglow aperture magnitudes are listed in Table 1. The photometric aperture radii are equal to the full width at half-maximum (FWHM) for each image, and background subtraction was performed using annuli around these apertures. The aperture positions were anchored to the same point, relative to field objects, in each image. The K_{E1} afterglow centroid was used as the reference position. Photometry was calibrated against UKIDSS (Lawrence et al. 2007) in *J*, *H*, and *K*, and Pan-STARRS (Chambers et al. 2016) in *r* and *Y*. All magnitudes are given in the AB system and are corrected for foreground Galactic dust extinction using an $R_V = 3.1$ Fitzpatrick reddening law (Fitzpatrick 1999) and the dust maps of Schlafly & Finkbeiner (2011), with $E(B - V) = 0.0165$. An afterglow was securely detected in the *J*, *H*, and *K*-band images, at a location consistent with that of the X-ray afterglow detected by *Swift*/XRT.

2.2 Hubble space telescope

The burst region was observed with Wide Field Camera 3[2] in the F606W and F160W bands on 2010 December 06 (10 months post-burst, programme 11840, PI: Levan). These bands have effective wavelengths of 0.57 and 1.52 μm, respectively. A three-point dither pattern was observed in each band, with total integration times of 1209 s (F160W) and 1140 s (F606W). ASTRODRIZZLE (part of the DRIZZLEPAC python package[3]) was used to reduce the images. The chosen PIXFRAC was 0.8, with final scales of 0.065 arcsec pixel^{-1} (F160W) and 0.02 arcsec pixel^{-1} (F606W).

We once again use the Gemini K_{E1} detection as a reference position, determining the burst location in the *HST* images by calculating a direct transformation based on six reference objects in the field. We use the IRAF tasks GEOMAP and GEOXYTRAN to fit for rotation, shifts and scaling in the *x* and *y* directions. The total positional uncertainty on the afterglow position in the *HST* frame has contributions arising from this transformation and the uncertainty on the afterglow position in the Gemini image, yielding a positional uncertainty of 18 mas in the F160W image and 49 mas in F606W. Fig. 2 shows image cutouts centred on the burst location. The source is not detected in either band. At the position of the afterglow, we measure 3σ magnitude limits of 26.7 in F160W and 27.1 in F606W (with a 0.4 arcsec aperture, for which STScI tabulate zero-points[4]). A similarly deep optical limit was obtained by Perley et al. (2010) 2 d post burst, using the Low Resolution Imaging Spectrometer on

[2]http://www.stsci.edu/hst/wfc3
[3]http://drizzlepac.stsci.edu
[4]http://www.stsci.edu/hst/wfc3/analysis

Keck (Oke et al. 1995) to place an *r*-band 3σ limit of 26.7 on any host emission at the burst location.

3 INTERPRETATION

In Fig. 3, we show the light curve for GRB 100250A, featuring the gamma-ray, X-ray, near-infrared (NIR), and *r*-band fluxes and limits. The prompt emission light curve, detected by the BAT instrument in gamma-rays, is characterized by a weak single peak with a duration of $T_{90} = 26.0 \pm 7.5$ s. There is no evidence for continued central engine activity beyond this period, and the X-ray is not sufficiently steep to be well explained as high-latitude emission. We therefore consider the possibility that the X-ray emission arises entirely from the afterglow forward shock. The X-ray light curve is monitored from a few minutes after the burst. It decays rapidly – the decay rate of $\sim t^{-2}$ at this early epoch is steeper than typically seen – becoming undetectable after about 30 min, before the first optical observation is made. The initial *r*-band non-detection lies chronologically between the X-ray monitoring and the start of NIR observations at about 3 h post burst. While the NIR data are sparse, it appears to show a less rapid decline in flux density than that seen in the X-ray. As a result, the X-ray to optical spectral energy distribution (SED) is difficult to reconstruct since there is no time overlap, and we consider two different methods for extrapolating between data points. In Figs 4 and 5, we construct SEDs from the afterglow measurements. The first assumes that the NIR and optical flux decays at the same rate as the X-ray, the second derives a decay rate from the two *K*-band points. We note that an extrapolation based on the prompt gamma-ray emission would lie between these, but is likely inappropriate for the late time afterglow. After considering the SED, we go on to discuss the burst energetics and the host non-detection.

3.1 X-ray based SED construction

First, we assume that the flux in *J*, *H*, and *K* bands shows the same time evolution as the X-ray flux, and that the flux decays according to $F_\nu \propto t^\alpha$. All detections and the *r*-band limit are extrapolated backwards or forwards to the mean time of the first epoch of observations (0.18 d, at which point there are contemporaneous NIR observations). The X-ray temporal slope $\alpha = -1.97 \pm 0.14$ and X-ray photon spectral index $\Gamma = 1.91^{+0.25}_{-0.22}$ are obtained from the *Swift* online data base[5] (90 per cent errors; Evans et al. 2009). The corresponding intrinsic neutral Hydrogen column density (at $z = 0$) is $(3^{+6}_{-3} \times 10^{20})$ cm^{-2}, a low value which disfavours a dusty, low-redshift explanation for the darkness of this GRB (Perley et al. 2010).

We extrapolate the X-ray flux to the optical (NIR) using a broken power law, with the two segments of the synchrotron spectrum given by $F_\nu \propto \nu^{-\Gamma+1}$ and $F_\nu \propto \nu^{-\Gamma+1+\Delta\beta}$, where $\Delta\beta$ accounts for a synchrotron spectral cooling break between the NIR and X-ray (Sari, Piran & Narayan 1998). $\Delta\beta = 0.5$ provides a satisfactory fit in most GRBs (Greiner et al. 2011).

The spectrum is fitted to the X-ray points, while the break frequency and break strength are allowed to vary. The parameter values that best fit the extrapolated NIR points are obtained through a procedure fully described in appendix A. The data are consistent either with an unbroken extrapolation ($\Delta\beta = 0$), or an extrapolation that breaks in the infrared (i.e. not shortwards of the *r*-band).

[5]http://www.swift.ac.uk/xrt_live_cat

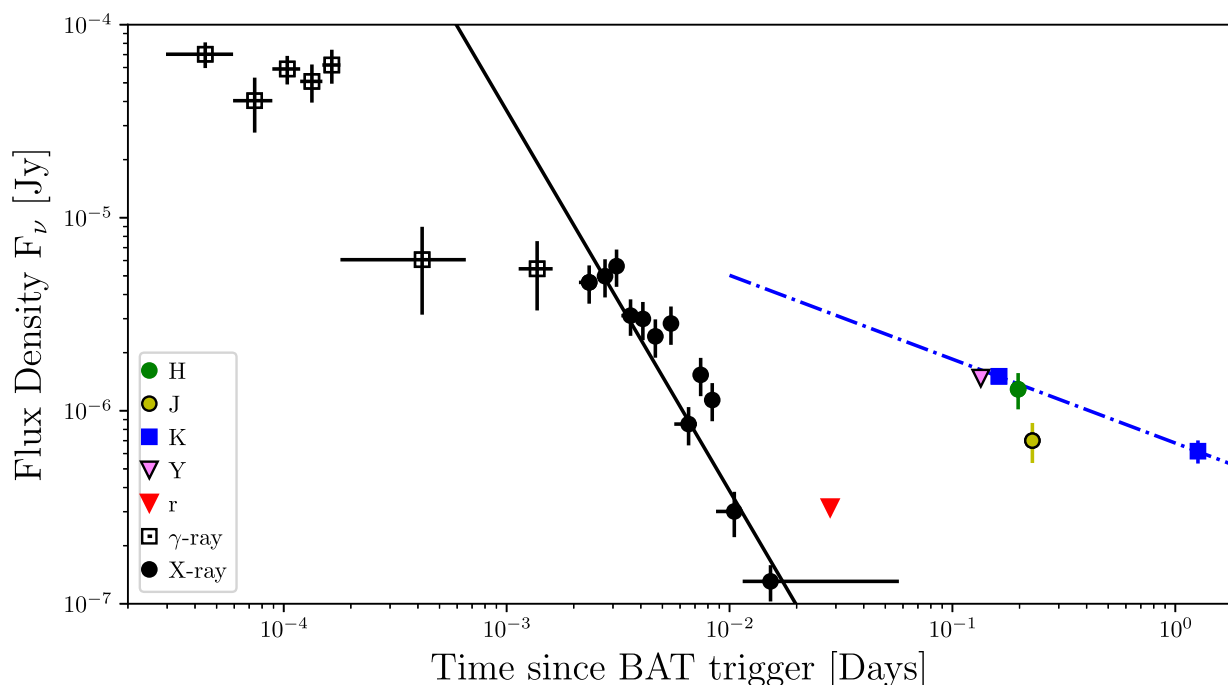**Figure 3.** The gamma-ray, X-ray, and NIR/optical light curve of GRB 100205A. Triangles represent 3σ upper limits, circles and squares are detections. The X-rays were undetected by *Swift* XRT by the time of the first optical/IR follow-up observation. The solid black line is a power law fit to the X-ray data points, representing the X-ray temporal decay, while the dashed blue line is a fit to the two *K*-band observations, giving the NIR decay rate. We do not extrapolate the NIR fit far beyond the *r*-band limit, as the prompt BAT light curve and NIR behaviour are likely driven by different physical mechanisms, making such a comparison misleading.

The upper panel of Fig. 4 illustrates the observed fluxes extrapolated in time as points with error bars and compares these against the $\Delta\beta = 0$ spectral extrapolation from the X-rays. The uncertainty in the X-ray extrapolation is indicated by the shaded region, which is dominated by the uncertainty on the XRT spectral slope.

The NIR to X-ray spectral slope, β_{IR-X}, is ~ -0.92, compared to the XRT value of -0.91 (where $\beta = 1 - \Gamma$). Fit values for this interpretation of the data are listed in Table 2. The fit in this case is very good given the uncertainties, although we note that the extrapolated K_{E2} point is not in agreement. Host contamination in the *K*-band is effectively ruled out by the deep *HST* non-detection in F160W, discussed in Section 3.4. Therefore, if the X-ray decay model is correct, then this epoch must have been contaminated by a flare or other non-standard variability.

Dark GRBs are typically classified based on X-ray to optical (i.e. *r*-band) rather than X-ray to NIR spectral slopes. GRB 100205A was classified as a dark burst with $\beta_{OX} < 0.28$, due to the very deep *r*-band non-detection at early times (Malesani et al. 2010). Given a simple power-law SED passing from the X-ray and through the optical limit, the NIR bands would also be expected to have a faint flux, inconsistent with the observations. In order to produce the observed *r*-band decrement relative to the X-ray to NIR fit described above, the spectrum would have to show a broken ($\Delta\beta > 0.5$) extrapolation from the X-ray to the *r*-band, followed by another sharp steepening of the slope in the narrow frequency range between *r* and *J* and a return to the original slope at longer wavelengths (lower frequencies) – i.e. three intrinsic spectral breaks in the afterglow. This is not consistent with any model or observation of GRB afterglow behaviour.

For the purposes of investigating the darkness of GRB 100205A, we instead adopt a simple case where the X-ray and NIR lie on the same section of the synchrotron spectrum ($\Delta\beta = 0$, or no break). We note that the best-fitting broken power law from Fig. A1, and this simplified model, are both consistent with the data.

Since many dark GRBs are the result of dust extinction (see for example Perley et al. 2009, 2013; Greiner et al. 2011; Svensson et al. 2012; Zauderer et al. 2013; Jeong et al. 2014a; van der Horst et al. 2015; Chrimes et al. 2019; Higgins et al. 2019), a first assumption may be that this apparent break is in fact due to spectral curvature induced by dust absorption within the host galaxy. The precise level of the relative dust correction between the observed *r* and *J* bands depends on the redshift of the source. Alternatively, the break could be due to the presence of the Lyman α break between the *r* and *J* bands (e.g. Kawai et al. 2006; Tanvir et al. 2009).

In order to determine the likely cause of the factor 100 drop in flux to the *r*-band, we compare a grid of afterglow models to the extrapolated NIR data points and *r*-band flux (for the latter we use the 1σ limit; see Table 2). The models consist of unbroken power laws with a range of β values given by the uncertainty on the XRT spectral slope. Each model is then placed at a range of redshifts ($0 < z < 7$), subject to a range of rest-frame dust attenuation ($0 < A_V < 3$, with an SMC-like attenuation law), and normalized to best fit the extrapolated NIR and *r*-band fluxes using χ^2 minimization. Because the *r*-band encroaches on the Lyman break from around $z \sim 4$, we account for the filter profile[6] and include the effect of line-of-sight averaged HI absorption as a function of redshift (Madau 1995; Madau & Haardt 2015). The results of minimizing χ^2 across the grid of parameters is shown in the lower panel of Fig. 4. The K, H, J, and *r*-bands are used for the fitting of four variables, however

---

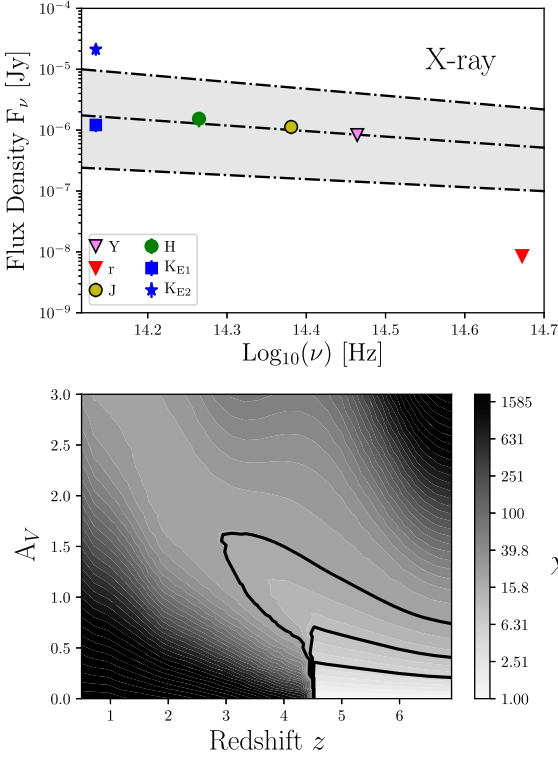[6]http://svo2.cab.inta-csic.es/svo/theory/fps

Figure 4. Upper panel: the afterglow SED for GRB 100205A, where the *J*, *H*, *K*, *Y*, and *r*-bands (triangles are 3σ upper limits) have been extrapolated to the midpoint of the first epoch of observations, assuming the same rate of dimming as measured in the X-rays. Flux uncertainties include the contribution from the uncertainty in temporal evolution. An extrapolation of the X-ray spectral slope with $\Delta\beta = 0$ at the same epoch is shown, with the 90 per cent confidence region shaded and bounded by dot-dash lines. A strong break occurs between *r* and *J*. Lower panel: χ^2 minimization over a grid of power law models. Contours representing the 67, 95, and 99.5 per cent frequentist probability intervals are overlaid in black.

these variables are not independent. We therefore conservatively assume only one degree of freedom, which defines the contours given the minimum in χ^2 (e.g. Avni 1976).

The result of this analysis is that the only region of parameter space producing acceptable fits is at high-redshift, and low dust extinctions. Because we see no evidence of the Lyman break entering the *J* band, we use the short-wavelength edge of this band ($\lambda \sim 1.17\,\mu m$) to infer an upper redshift limit of $\sim$8. This places GRB 100205A in the range $4.5 < z < 8$, at the high end of the GRB redshift distribution.

Another possibility is that molecular Hydrogen, vibrationally excited by a strong ultraviolet (UV) flux, could produce absorption at rest-frame UV wavelengths (shortwards of 1650 Å; Draine 2000; Sheffer et al. 2009; Wiersema et al. 2018). However, molecular to atomic Hydrogen ratios are sufficiently low in GRB hosts, even when H_2 lines are detected, that it effectively rules out this scenario (Bolmer et al. 2019).

3.2 NIR based SED construction

This analysis also suffers from uncertainty due to the assumed fading rate of the afterglow. For an alternative approach, we can look instead at the temporal decay of the afterglow in the *K*-band. The NIR temporal index $\alpha = -0.43 \pm 0.16$ (90 per cent error) is
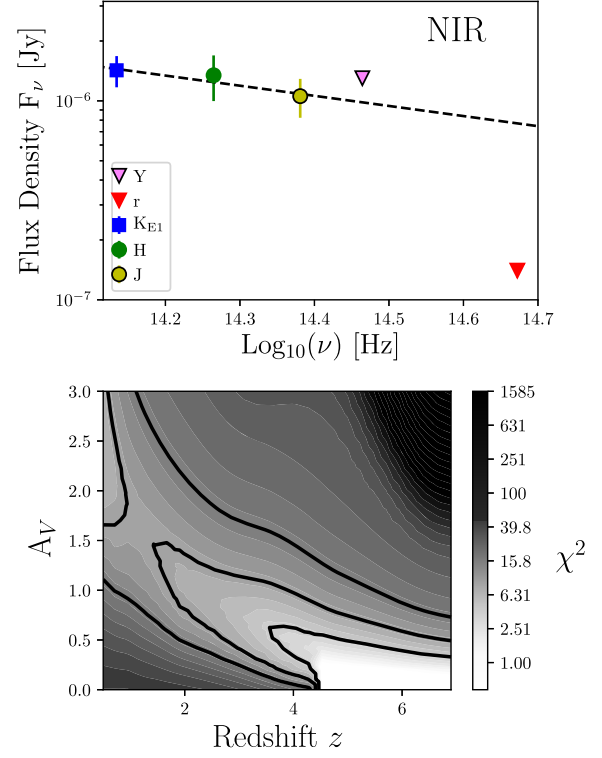

Figure 5. Upper panel: As in Fig. 4, but the fluxes and limits are extrapolated using the decay rate as seen in the *K*-band. The K_{E2} point is not shown as it overlaps with K_{E1} by construction. The best-fitting NIR spectral slope is given by the dashed line. Lower panel: χ^2 minimization as in Fig. 4, with data extrapolated according to the *K*-band decay rate.

substantially different from the X-ray temporal index, warranting an alternative interpretation of the data using this decay rate instead.

In the upper panel of Fig. 5, we extrapolate the *r*-limit and NIR fluxes to the epoch 1 mean time of 0.18 d using the *K*-band decay rate, and fit a spectral slope to the NIR points at that epoch. The best-fitting NIR spectral slope has the value $\beta_{NIR} = -0.51 \pm 0.26$ (90 per cent error). The break between *r* and *J* is less strong in this scenario, with a flux decrement of factor $\sim$5. Fit parameters are listed in Table 2, for ease of comparison to the X-ray decay interpretation.

A single spectral break between the *J* amd *r* bands could, in this case, explain the photometric data. In order to do this, however, extremely low environmental densities would be required to produce such a blue break frequency at $\sim$4–5 h post burst, and would be highly unusual (e.g. Wijers & Galama 1999; Greiner et al. 2011).

As for the X-ray hypothesis, we compare afterglow models to the extrapolated NIR data points and *r*-band flux in order to determine the possible cause of this spectral break. The models are once again power laws with a spread of β values, bounded by the uncertainty on the NIR spectral slope. The models are subject to a range of redshifts ($0 < z < 7$), dust attenuations ($0 < A_V < 3$), and normalizations. Neutral hydrogen absorption and the filter profile are accounted for as before. The lower panel of Fig. 5 shows the results of minimizing χ^2 over this parameter space. Although dusty and low-redshift scenarios cannot be ruled out, the 67 per cent confidence region is nearly entirely limited to $z > 4$ and $A_V < 0.5$, indicating a preference for low-dust, high-redshift solutions. The presence of emission in the *J*-band, as with the X-ray case, places an upper limit of $z < 8$ on the burst, putting it in the range $4 < z < 8$.

Table 2. Values of the parameters obtained from fitting power laws to the X-ray or temporally extrapolated NIR and optical data, assuming the fading rate of either the X-rays or *K*-band. Included are the temporal index α and spectral index β (with 90 per cent errors), extrapolated *r*-band limits, and the flux decrement F_d between the observed *r*-band (for which we use the 3σ *r*-band constraint) and the model.

	α	β	Extrapolated *r*-band $1 (3)\sigma$ limit [Jy]	F_d
X-ray	-1.97 ± 0.14	$-0.91^{+0.25}_{-0.22}$	$2.92 \, (8.50) \times 10^{-9}$	>64
K-band	-0.43 ± 0.16	-0.51 ± 0.26	$0.47 \, (1.40) \times 10^{-7}$	>5.5

Figure 6. The isotropic equivalent energy E_{iso} of *Swift* GRBs from the optically unbiased TOUGH sample versus redshift. GRB 100205A (indicated by the red line) is not unreasonably under-luminous at any redshift $\gtrsim 0.5$, and not unreasonably luminous at any redshift. Energetics considerations therefore cannot rule out a high-redshift interpretation.

Figure 7. GRB host galaxy apparent magnitudes, measured in the *HST* F160W band (Blanchard et al. 2016; Lyman et al. 2017; Chrimes et al. 2019). Four high-redshift GRB host detections in the *J* and F140W bands, and two 2σ upper limits (F160W, triangles), are also shown (Tanvir et al. 2012; McGuire et al. 2016). The $2\sigma (3\sigma)$ limit at the position of GRB 100205A is indicated with a dashed (solid) line.

We cannot rule out variability in the NIR, particularly as there are only two epochs available in the *K*-band. We note that the disagreement between the X-ray and NIR temporal slopes might indicate that there is non-afterglow activity occurring in either band. We can likely be confident that the correct decay rate and spectral slope lie somewhere between the NIR and X-ray cases. The non-standard X-ray afterglow argument is strengthened if the burst is indeed at high-redshift – given that the X-ray observations finished at $t \sim 40$ min, this corresponds to only a few minutes post burst in the rest-frame (for $4 < z < 8$). Such early times often show non-standard afterglow activity, including flares, the decay of which could produce the steep X-ray decline seen in this burst (Nousek et al. 2006).

The result that the burst lies in the range $4 < z < 8$ is independent of the method chosen to interpret these data as Figs 4 and 5 demonstrate.

3.3 High energy properties

The high energy properties of GRB 100205A can also offer some constraints. In particular, a bright burst may become a significant outlier in energetics at higher redshift, disfavouring such a distance indication. Fig. 6 shows the distribution of isotropic energy inferred for *Swift* GRBs from the optically unbiased TOUGH sample against redshift (Hjorth et al. 2012). GRB 100205A is unremarkable if placed at any redshift $\gtrsim 0.5$, although it is at the fainter end of the luminosity distribution. The energetics of GRB 100205A therefore do not preclude a high-redshift interpretation.
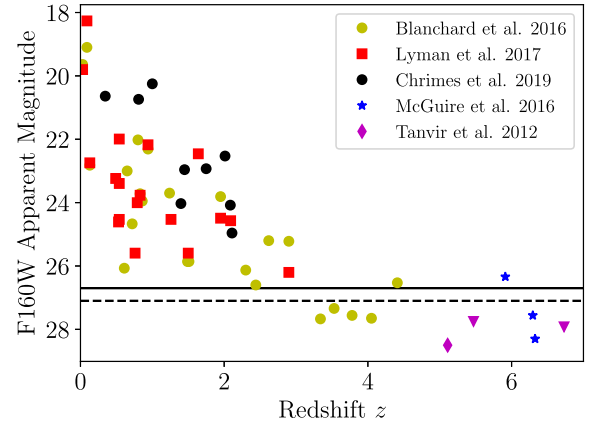
3.4 Non-detection of the host

Finally, the extremely deep limit obtained for the galaxy host flux in the *HST* F160W band strongly favours a higher redshift origin. This is not due to the Lyman break – this feature is not redshifted into the F160W filter until $z \sim 11 - 12$, and at redshifts this high no *J* or *H*-band afterglow detection would be expected. The NIR afterglow detections in fact provide a firm upper limit on the redshift of $z \sim 8$. Instead, the host non-detection implies a very low intrinsic host luminosity rather than HI absorption in the intergalactic medium.

In Fig. 7, we show F160W apparent magnitudes for GRB hosts with known redshift (either from host emission or afterglow absorption lines; Blanchard, Berger & Fong 2016; Lyman et al. 2017; Chrimes et al. 2019). We also include three high redshift data points in F140W – GRBs 130606A, 050904, and 140515A (McGuire et al. 2016) – in addition to one detected host (GRB 060522, *J*-band) and two deep limits (F160W) from Tanvir et al. (2012). The Lyman et al. (2017) sample is composed exclusively of optically bright (thus $z < 3$) bursts. The Chrimes et al. (2019) sample is composed exclusively of dark bursts. The other samples include a mixture of bursts. For redshifts $z \lesssim 3$, an apparent 1–2 µm (observed) magnitude of >26.7 is uncharacteristically faint for GRB hosts, and at these lower redshifts essentially all are detected. Conversely, at $z \gtrsim 3$, such faint hosts become the norm, with most host galaxies undetected at this level. We note that in the sample of Chrimes et al. (2019), GRB 100205A is the *only* burst for which no host is detected in F160W. If we assume that GRB 100205A occurred

at $z = 5$, the rest-frame UV absolute magnitude of the host is $M_{UV} > -19.74$, placing it at least one magnitude fainter than M_* at that redshift (Bouwens et al. 2015) – demonstrating the ability of GRBs to select low-mass star forming galaxies in the distant Universe.

4 CONCLUSIONS

We have presented Gemini and *HST* imaging of the afterglow and host galaxy location of the dark GRB 100205A. The lack of a detected host at m_{AB}(F160W) > 26.7 ($3\,\sigma$), combined with a strong spectral break in the afterglow SED between r and J, suggests a high-redshift ($4 < z < 8$) origin for this burst, adding it to the small sample of GRBs known to have occurred in the early Universe. Despite the limited photometric coverage, this conclusion stands independent of the spectral and temporal extrapolation methods assumed. It was only identified thanks to rapid and deep optical observations that could place meaningful constraints on the darkness of a burst with an apparently faint X-ray afterglow, and subsequently inform infrared observations. This highlights that such deep observations, beyond the range of modest aperture telescopes at any epoch, may well be necessary to significantly increase the sample of known high-redshift GRBs.

REFERENCES

Afonso P. et al., 2011, A&A, 526, A154
Avni Y., 1976, ApJ, 210, 642
Barthelmy S. D. et al., 2005, Space Sci. Rev., 120, 143
Berger E. et al., 2007, ApJ, 665, 102
Blanchard P. K., Berger E., Fong W.-. fai., 2016, ApJ, 817, 144
Bolmer J. et al., 2019, A&A, 623, A43
Bouwens R. J. et al., 2015, ApJ, 803, 34
Burrows D. N. et al., 2004, in Flanagan K. A., Siegmund O. H. W., eds, Proc. SPIE Conf. Ser. Vol. 5165, X-Ray and Gamma-Ray Instrumentation for Astronomy XIII, SPIE, Bellingham, p. 201
Casali M. et al., 2007, A&A, 467, 777
Castro-Tirado A. J. et al., 2013, GCN Circ. No. 14796, #1
Cenko S. B., Berger E., Djorgovski S. G., Mahabal A. A., Fox D. B., 2006, GCN, 5155, 1
Chambers K. C. et al., 2016, preprint (arXiv:1612.05560)
Chornock R., Berger E., Fox D. B., Fong W., Laskar T., Roth K. C., 2014a, preprint (arXiv:e-prints)
Chornock R., Fox D. B., Berger E., 2014b, GCN Circ., No. 16269, #1
Chrimes A. A. et al., 2019, MNRAS, 486, 3105
Cobb B. E., Cenko S. B., Bloom J. S., 2010, GCN Circ., No. 10365, #1
Cucchiara A., Fox D. B., Tanvir N. R., Levan A. J., Cobb B. E., Berger E., Chornock R., 2010, GCN Circ., No. 10374, #1
Cucchiara A. et al., 2011, ApJ, 736, 7
Draine B. T., 2000, ApJ, 532, 273
Evans P. A. et al., 2009, MNRAS, 397, 1177
Fitzpatrick E. L., 1999, PASP, 111, 63
Fruchter A. S., 1999, ApJ, 512, L1
Fynbo J. U. et al., 2001, A&A, 369, 373
Gehrels N. et al., 2004, ApJ, 611, 1005
Grazian A. et al., 2006, GCN Circ. 4545
Greiner J. et al., 2009, ApJ, 693, 1610
Greiner J. et al., 2011, A&A, 526, A30
Groot P. J. et al., 1998, ApJ, 502, L123
Hambly N. C. et al., 2008, MNRAS, 384, 637
Hartoog O. E. et al., 2015, A&A, 580, A139
Hewett P. C., Warren S. J., Leggett S. K., Hodgkin S. T., 2006, MNRAS, 367, 454
Higgins A. B. et al., 2019, MNRAS, 484, 5245
Hjorth J. et al., 2012, ApJ, 756, 187
Hodapp K. W. et al., 2003, PASP, 115, 1388
Hodgkin S. T., Irwin M. J., Hewett P. C., Warren S. J., 2009, MNRAS, 394, 675
Hook I. M., Jørgensen I., Allington-Smith J. R., Davies R. L., Metcalfe N., Murowinski R. G., Crampton D., 2004, PASP, 116, 425

Jakobsson P., Hjorth J., Fynbo J. P. U., Watson D., Pedersen K., Björnsson G., Gorosabel J., 2004, ApJ, 617, L21

Jakobsson P. et al., 2006, in Holt S. S., Gehrels N., Nousek J. A., eds, AIP Conf. Proc. Vol. 836, Gamma-Ray Bursts in the Swift Era. Am. Inst. Phys., New York, p. 552

Jeong S. et al., 2014a, A&A, 569, A93

Jeong S., Sanchez-Ramirez R., Gorosabel J., Castro-Tirado A. J., 2014b, GCN Circ., No. 15936, #1

Kawai N. et al., 2006, Nature, 440, 184

Laskar T. et al., 2014, ApJ, 781, 1

Lawrence A. et al., 2007, MNRAS, 379, 1599

Levan A. et al., 2006, ApJ, 647, 471

Lyman J. D. et al., 2017, MNRAS, 467, 1795

Madau P., 1995, ApJ, 441, 18

Madau P., Haardt F., 2015, ApJ, 813, L8

Malesani D., Xu D., Fynbo J. P. U., Jakobsson P., Tanvir N. R., Lindberg J., 2010, GCN Circ., No. 10362, #1

McGuire J. T. W. et al., 2016, ApJ, 825, 135

Nicuesa A., Kruehler T., Rossi A., Greiner J., 2010, GCN Circ., No. 10383, #1

Nousek J. A. et al., 2006, ApJ, 642, 389

Oke J. B. et al., 1995, PASP, 107, 375

Perley D. A. et al., 2009, AJ, 138, 1690

Perley D. A., Bloom J. S., Cenko S. B., Cobb B. E., Morgan A. N., Miller A. A., Klein C. R., 2010, GCN Circ., No. 10399, #1

Perley D. A. et al., 2013, ApJ, 778, 128

Racusin J. L. et al., 2010, GCN Circ., No. 10361, #1

Ruiz-Velasco A. E. et al., 2007, ApJ, 669, 1

Salvaterra R. et al., 2009, Nature, 461, 1258

Sari R., Piran T., Narayan R., 1998, ApJ, 497, L17

Schlafly E. F., Finkbeiner D. P., 2011, ApJ, 737, 103

Sheffer Y., Prochaska J. X., Draine B. T., Perley D. A., Bloom J. S., 2009, ApJ, 701, L63

Sparre M. et al., 2014, ApJ, 785, 150

Svensson K. M. et al., 2012, MNRAS, 421, 25

Tanvir N. R. et al., 2009, Nature, 461, 1254

Tanvir N. R., Levan A. J., Cucchiara A., Fox D., Cobb B. E., Mason R., 2010, GCN Circ., No. 10366, #1

Tanvir N. R. et al., 2012, ApJ, 754, 46

Tanvir N. R. et al., 2018, ApJ, 865, 107

Trenti M., Perna R., Levesque E. M., Shull J. M., Stocke J. T., 2012, ApJ, 749, L38

Urata Y., Huang K. Y., Im M., 2010, GCN Circ., No. 10375, #1

van der Horst A. J. et al., 2015, MNRAS, 446, 4116

van der Horst A. J., Kouveliotou C., Gehrels N., Rol E., Wijers R. A. M. J., Cannizzo J. K., Racusin J., Burrows D. N., 2009, ApJ, 699, 1087

Wiersema K. et al., 2018, MNRAS, 481, 1126

Wijers R. A. M. J., Galama T. J., 1999, ApJ, 523, 177

Wright E. L., 2006, PASP, 118, 1711

Zauderer B. A. et al., 2013, ApJ, 767, 161

APPENDIX: FITTING THE X-RAY TO NIR SED

In this appendix we detail the fitting procedure used to determine the best spectral fit to the NIR data, given a temporal and spectral
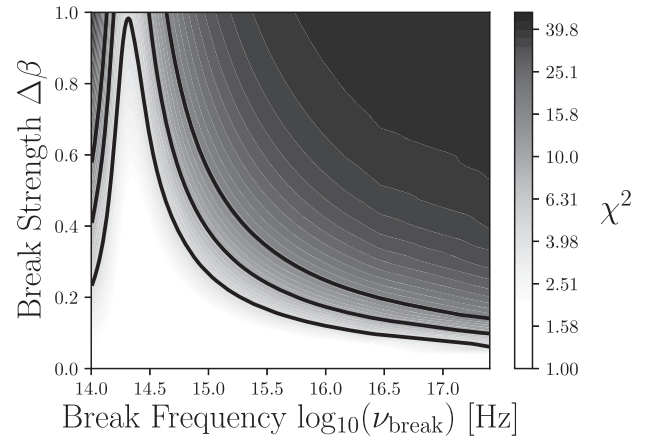

Figure A1. The result of fitting a broken power law to the *J*, *H*, *K*, and X-ray fluxes through χ^2 minimization. One, two, and three σ contours are shown (Avni 1976). The power-law models are fixed to the X-ray data, but we allow for a range of break frequencies and strengths at lower energies. A break in the NIR is favoured, and the possibility that the NIR and X-ray points lie on the same section of the synchrotron spectrum is not excluded.

extrapolation from the X-ray, as outlined in Section 3.1. A broken power-law model is used, extrapolated from the X-ray using the *Swift*/XRT spectral slope, until a break frequency ν_{break} is reached (Sari et al. 1998). At this break frequency, the spectral slope shallows by an amount $\Delta\beta$, allowed to vary between 0 and 1, covering a representative range (this break normally occurs between the X-ray and optical, see e.g. Greiner et al. 2011). We fit a broken power law from the X-ray to the *J*, *H*, and *K* points, covering a range of break frequencies and break strengths. Minimizing χ^2 over this parameter space produces best-fitting values of $\log_{10}(\nu_{break}) = 14.24$, between the *K* and *H* bands, and a strength $\Delta\beta = 0.73$. The range of statistically acceptable fits within 67, 95, and 99.5 per cent confidence regions is shown in Fig. A1.

The flux decrement between the (time-extrapolated) *J* and the *r*-band is independent of whether a simple $\Delta\beta = 0$ spectral extrapolation is used (which is consistent within the uncertainties), or if the best fit from this procedure is used (where a break is included longwards of this filter). This suggests that the *r*-band non-detection is due to dust or the Lyman-break at high redshift, rather than an afterglow-related spectral break.

This paper has been typeset from a TeX/LaTeX file prepared by the author.